Pterodactyl: Development and Comparison of Control Architectures for a Mechanically Deployed Entry Vehicle

Wendy A. Okolo*, Benjamin W. Margolis†, Sarah N. D'Souza‡

NASA Ames Research Center, Moffett Field, CA 94035, USA

Jeffrey D. Barton§

John Hopkins University Applied Physics Laboratory, Laurel, MD, 20723

Abstract

The Pterodactyl project, seeks to advance the current state-of-the-art for entry vehicles by developing novel guidance and control technologies for Deployable Entry Vehicles (DEVs) that can be applied to various entry vehicle configurations. This paper details the efforts on the NASA-funded Pterodactyl project to investigate and implement multiple control techniques for an asymmetric mechanical DEV. We design multiple control architectures for a Pterodactyl Baseline Vehicle (PBV) and evaluate their performance in achieving varying guidance commands during entry. The control architectures studied are (i) propulsive control systems such as reaction control systems and (ii) non-propulsive control systems such as aerodynamic control surfaces and internal moving masses. For each system, state-feedback integral controllers based on linear quadratic regulator (LQR) optimal control methods are designed to track guidance commands of either (i) bank angle or (ii) angle of attack and sideslip angle as determined by the desired guidance trajectory. All control systems are compared for a lunar return reference mission and by providing a comparative analysis of these systems, configurations, and performance, the efforts detailed in this paper and the Pterodactyl project as a whole will help entry vehicle system designers determine suitable control architectures for integration with DEVs and other entry vehicle types.

I.   Introduction

Pterodactyl is a NASA-funded design and test capability to (i) advance the current state of the art for entry vehicle guidance and control (G&C) and (ii) determine the feasibility of control system integration for various entry vehicle types. A deployable Entry Vehicles (DEV) is a type of unconventional entry vehicle that demonstrates significant promise for enabling new missions including sample return missions and high-mass payload delivery. Because they have no back shell, a DEV can stow into a smaller volume for launch and deploy prior to entry. This novelty in their design, results in challenges in developing and integrating feasible guidance and control solutions for entry, descent, and landing. Thus, the Pterodactyl capability, driven and funded by NASA's Space Technology Mission Directorate (STMD) is being utilized to develop novel hardware and software G&C solutions for DEVs that will enable their use in existing and future space missions as demonstrated for a sample return mission in this paper [1].

To advance the state of the art for entry vehicle guidance and control, the Pterodactyl project is (i) designing and integrating unconventional control hardware architectures onto a DEV and (ii) developing and applying novel guidance and control algorithms for the vehicle to utilize the control hardware designs in flight [1]. The current state of the art for entry vehicle control hardware utilizes reaction control systems

---

*Aerospace Research Engineer, Intelligent Systems Division, MS 269-1, AIAA Member
†Graduate Pathways Student, Systems Analysis Office, MS 258-1, AIAA Member
‡Principal Investigator, Systems Analysis Office, MS 258-1, AIAA Member
§Guidance & Control Engineer, Force Projection Sector, JHU/APL, Non-Member

American Institute of Aeronautics and Astronautics

(RCS) for rigid entry vehicles such as the Mars Science Laboratory (MSL), Apollo capsule, and the Space Shuttle [2]. These reaction control systems consist of a set of thrusters mounted on the backshells of the rigid vehicles to steer them during entry. Since DEVs have no backshell, mounting RCS thrusters is a non-trivial hardware integration challenge. Thus, the Pterodactyl effort is investigating the feasibility of integrating not just RCS on a DEV, but unconventional control architectures such as (i) moving masses to control the vehicle by changing it's center of gravity (CG) and inertia and (ii) aerodynamic control effectors to control the vehicle by generating aerodynamic moments. These two techniques, untraditional for entry vehicles, have been demonstrated in other aerospace vehicle applications such as in aircraft formation flight for fuel savings in which Okolo et al [3] utilized internal fuel transfer to generate roll moments to trim an aircraft by changing it's CG and inertia matrix. Furthermore, aerodynamic control surfaces such as elevators, ailerons, and rudders, are routinely used to generate pitch, roll, and yaw aerodynamic moments, respectively, to trim and steer aircraft. Single flap designs have also been demonstrated for entry vehicle systems such as the Mid L/D vehicle [4] for which control surfaces and reaction control systems were utilized to generate moments.

In terms of the software solutions being developed by Pterodactyl, it is important to understand the traditional guidance and control algorithms utilized by heritage entry vehicles. Heritage entry vehicles utilize a bank-angle guidance scheme to modulate the lift vector and control the downrange and crossrange errors in a coupled fashion, while relying on the vehicle's natural trim angle of attack based on the vehicle's center of gravity (CG) location at launch. Mitigating these downrange and cross-range errors and guiding the vehicle along a trajectory during entry with limited tuning knobs can be a challenge for the guidance system as it has to determine when to change the bank angle and thus lift vector to reduce these errors [1]. Conducting these bank reversals introduces errors due to rate and acceleration limits of the control system effecting these guidance commands. Pterodactyl has developed a guidance capability that uncouples longitudinal and lateral/directional forces allowing for independent downrange and crossrange guidance commands through direct angle of attack modulation for downrange control and sideslip modulation for cross-range control [5]. This provides G&C solutions that can allow for traditional bank angle or uncoupled angle of attack and sideslip guidance commands to be followed by a control system.

Furthermore, heritage entry vehicles have typically used classical control methods such as proportional-integral-derivative (PID) controllers and other variants to achieve guidance commands [6, 7]. The design process using these classical techniques involves analyzing the stability of the vehicle and designing a controller that can (i) stabilize the vehicle by moving the poles of the system to the left-hand side of the imaginary plane and (ii) control the vehicle to follow commands by determining a suitable control gain that will drive the errors between the commanded and true signals to zero. These methods provide good stability characteristics and do not have high computational requirements but require linear time invariant (LTI) system dynamics and do not provide a platform to achieve optimal predefined objectives such as minimal control effort over an entire trajectory. Thus, the Pterodactyl controls approach is to utilize optimal modern control methods, specifically linear quadratic regulator (LQR) control design for each unconventional hardware architecture presented in this paper. This provides the capability to develop a robust controller that stabilizes and controls the vehicle in an optimal fashion while balancing pre-defined control effort usage and vehicle performance requirements. The analysis and evaluation of the control designs form the brunt of the work presented in this paper.

First, we give an overview of the reference re-entry mission, the baseline vehicle, and the three control hardware architectures in Section II. In Section III, we describe the integrated Python simulation environment developed to simulate the vehicle and evaluate the controller responses. This is followed by the control design for all three control architectures in Section IV after which we analyze the vehicle's stability and controllable operating regimes in Section V. The implications of this analysis drive a controller development and evaluation for the three control architectures in Section VI. This is followed by conclusions and a guide to future work in Section VII.

II.   Mission, Vehicle, & Control Architectures

The scope of Pterodactyl is in developing the G&C capabilities for the entry phase of a DEV conducting a lunar return mission as described by D'Souza et al in Ref. [1]. To this effect, descent and landing technologies are not considered or evaluated for this study as the effort is focused on the G&C technologies that can enable precision targeting considering the aerodynamic and heating rates resulting from high Earth entry speeds down to descent initiation at Mach 2. A peak heat flux of 250 W/cm2 is assumed based on the proven

American Institute of Aeronautics and Astronautics

capability of the vehicles's thermal protective system, and g-loads below 15 g?s are considered based on anticipated payload sensitivity to deceleration loads. Additionally, a secondary payload envelope on the Aft Bulkhead Carrier (ABC) of a Centaur V is utilized as a constraint for mass and volume for G&C designs, resulting in an assumed volume of 0.5 m x 0.5 m x 0.6 m and mass of 77 kg for the baseline vehicle [1, 8].

The Pterodactyl Baseline Vehicle (PBV), the DEV used to demonstrate the integrated G&C solutions, is based on the Lifting Nano-ADEPT (LNA) [9], an asymmetric variant of the ADEPT (Adaptable, Deployable, Entry Placement Technology) vehicle [10]. The PBV has a flexible thermal protection system (TPS) that can be stowed during launch and deployed prior to or during entry [11]. This vehicle, depicted in Fig. 1, has a nominal 1-meter diameter with two longer ribs on the trailing edge side of the vehicle to create an asymmetric surface and generate lift. In the lift-up configuration, these longer trailing edge ribs point downward; thus to increase lift, the vehicle pitches down and increases angle of attack in the negative direction. The reverse is the case - to decrease lift, the vehicle pitches up and increases angle of attack in the positive direction. To control the vehicle, we investigate three control architectures - Flap Control System (FCS), Reaction Control System (RCS), and Mass Movement Control System (MMCS). These architectures are independently integrated with the vehicle as depicted in Fig. 2 and brief overviews of the three control systems are given in Sections A through C. For additional details on the PBV and the control system hardware integration, Ref. [12] should be consulted.
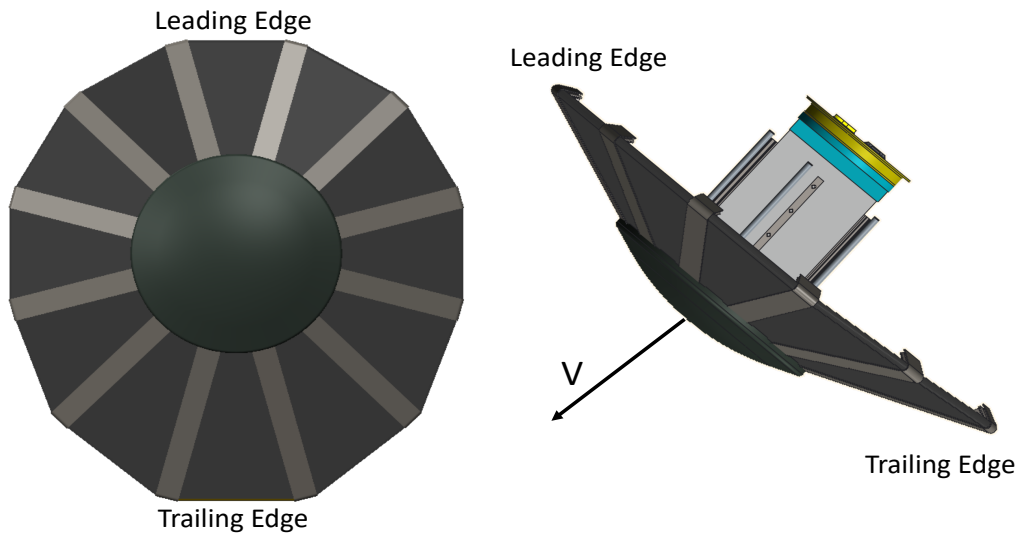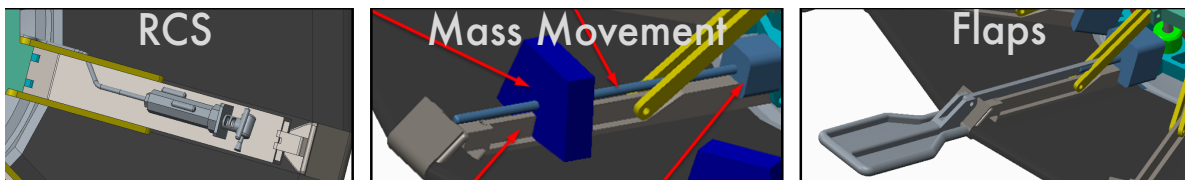

Figure 1. Pterodactyl Baseline Vehicle

Figure 2. Control Hardware Architectures

A. Flap Control System (FCS)

Eight aerodynamic control surfaces, sized to provide maximum control authority while meeting packaging and stowing constraints [1], were affixed to eight of the ribs as depicted in Fig. 3. These flaps were designed to provide the capability to follow (i) decoupled angle of attack and sideslip guidance commands and (ii) bank angle guidance commands if necessary. The longitudinal flaps (1, 2, 7, and 8) are designed to provide primarily pitch control by changing the vehicle's angle of attack while the lateral tabs (3 - 6) are
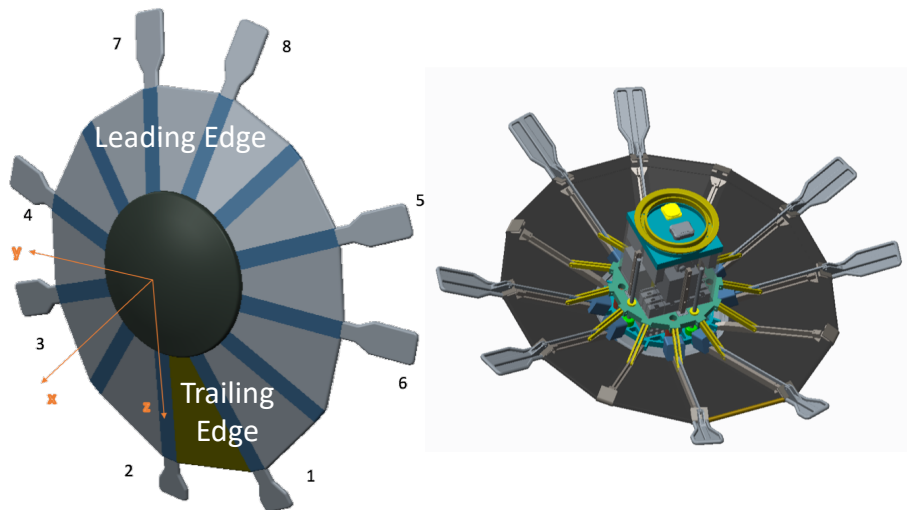
Figure 3. Fore and aft views of the PBV with control surfaces

designed primarily for yaw control through sideslip modulation. Deflecting longitudinal tabs 1 and 2 into the flow generates a negative/downwards pitch moment while doing the same for tabs 7 and 8 generates a positive/upwards pitch moment. When deflected into the flow, tabs 3 and 4 yaw the vehicle right while tabs 5 and 6 create a left yaw orientation. All tabs have a maximum of 20° deflection into the flow ($+20°$) and 45° retraction (-45°) out of the flow due to in-flight aerothermal limits and mechanical design integration constraints, respectively [12, 13].

B. Reaction Control System (RCS)

As shown in Fig. 4, four thrusters are mounted on the lateral ribs - the ribs on which the control surfaces 3-6 are affixed in the previous design . These thrusters fire in pairs and can independently generate 1N thrust magnitudes. They are designed to provide roll control to change the vehicle's orientation and track bank angle guidance commands. Firing a pair of thrusters located on one side of the x-z plane will roll the vehicle in one direction and change the bank angle while firing the opposite thruster pair rolls the vehicle in the other direction and generates a bank reversal [12].
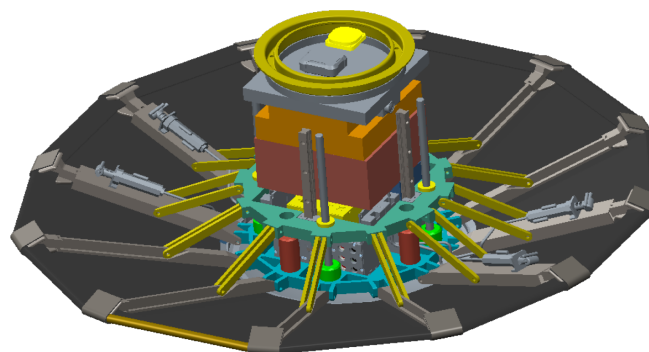

Figure 4. PBV depicting four reaction thrusters

C. Mass Movement Control System (MMCS)

Similar to the flap design, eight 2 kg movable masses are integrated on eight ribs with maximum weights chosen to meet packaging requirements [12]. These masses, depicted on the LNA in Fig. 5 are designed

American Institute of Aeronautics and Astronautics

to provide control of either angle of attack and sideslip or the bank angle, depending on the guidance requirements. Unlike the flaps which generate aerodynamic moments when deflected into and out of the flow, or the RCS that directly generates torques from thrusters, the moving mass system changes the vehicle CG and inertia matrix by redistributing weight primarily in the y-z plane of the vehicle. This implies that the CG shift realizable with this architecture is in the y and z directions primarily. As a result, this control architecture will be investigated for angle of attack and sideslip control primarily.
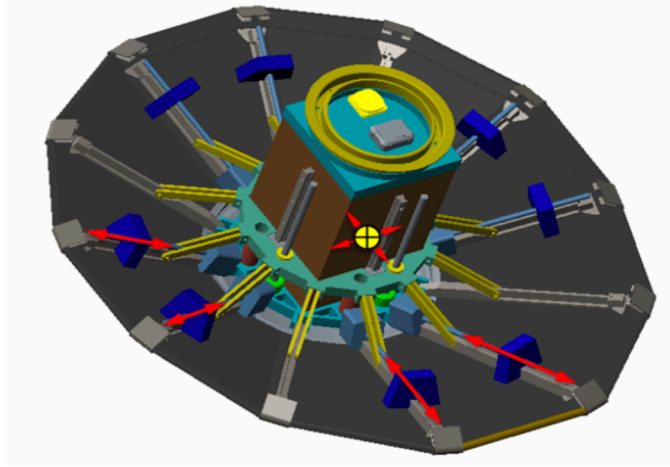

Figure 5. PBV depicting eight movable masses

III.   Simulation Development

In this section, we give an overview of the Python-based simulation environment developed to simulate the vehicle and evaluate the control design. First we briefly describe the aerodynamic model of the PBV and how it is represented and utilized in simulation, after which we present the equations of motion for the different control architectures. For extensive details on developing the integrated simulation framework, the previous publications of the authors [14,15] should be consulted.

A.   Aerodynamic Model

The aerodynamic forces and moments, F, and M respectively, can be represented as:

$$F = \bar{q} S_A C_F$$
$$M = \bar{q} S_A \, \bar{c} \, C_M \tag{1}$$

respectively, where S_A is the reference surface area, $\bar{c}$ is a reference length, and $\bar{q}$ is the dynamic pressure. Furthermore, C_F and C_M are the dimensionless aerodynamic force and moment coefficients respectively, and can be represented as:

$$C_F = C_{F,PBV}\left(\alpha, \beta, M\right) + \Delta C_{F,ACS}\left(\delta_1, \ldots, \delta_8\right)$$
$$C_M = C_{M,PBV}\left(\alpha, \beta, M\right) + \Delta C_{M,ACS}\left(\delta_1, \ldots, \delta_8\right) \tag{2}$$

where $C_{F,PBV}$ and $C_{M,PBV}$ are the aerodynamic force and moment coefficients respectively on the base vehicle, due to its orientation (i.e. angle of attack and sideslip) and operating environment (i.e. Mach number). $\Delta C_{F,ACS}$ and $\Delta C_{M,ACS}$ are the incremental aerodynamic force and moment coefficients on the vehicle induced only by the aerodynamic control surfaces (ACS). This implies that, for the two configurations with no aerodynamic surfaces - reaction control system and moving mass system - the $\Delta C_{F,ACS}$ and $\Delta C_{M,ACS}$ terms are automatically zero in the aerodynamic model.

The aerodynamic force and moment coefficients were generated using Cart3D for a matrix of flight conditions from the expected flight envelope [13] . Table 1 shows the flight conditions used to develop the database. To utilize the data in analysis and simulation, multivariate B-splines [16,17] were constructed to smoothly interpolate the aerodynamic database at any Mach, angle of attack, sideslip, and control surface

American Institute of Aeronautics and Astronautics

deflections. The interpolating spline curves were also differentiated to obtain dimensionless stability deriva-
tives such as the dihedral effect, pitch, stiffness, and yaw stiffness, to understand the stability characteristics
and limitations of the vehicle. Additional details are given in Ref. [14, 15].

Table 1. Flight Conditions for Aerodynamic Database Generation

Independent variable	Values
Mach number M	$\{40, 31, 20, 15, 10, 5, 2\}$
Angle-of-attack α, deg	$\{0, \pm5, \pm10, \pm15, \pm20\}$
Sideslip angle β, deg	$\{0, \pm5, \pm10, \pm20\}$
Control surface deflection δ_i, deg	$\{-45, -20, 0, 10, 20, 30\}$

B.   Equations of Motion

For this study, we utilize previously developed equations of motion of a hypersonic re-entry vehicle as
described by Vinh [18]. We present the final forms of the linear and angular dynamics and kinematics
equations for the PBV independently integrated with the FCS, RCS, and MMCS control architectures.

The linear dynamics are given by

$$
\begin{aligned}
\dot{V} &= -\frac{g(z)}{m} \sin(\gamma) - \frac{1}{m} D \\
\dot{\gamma} &= \left(-\frac{g(z)}{mV} + \frac{V}{z} \right) \cos(\gamma) \\
&\quad + \frac{1}{mV} (L \cos(\sigma) - S \sin(\sigma)) \\
\dot{\xi} &= \frac{1}{mV \cos(\gamma)} (L \sin(\sigma) + S \cos(\sigma))
\end{aligned}
\tag{3}
$$

where V is the velocity of the vehicle, γ is the vehicle flight-path angle, ξ is the vehicle heading angle defined
from due North, L, D, and S are the aerodynamic lift, drag, and side forces, respectively, $g(z)$ is the force
due to gravity, dependent on the radial distance from the planet center z, σ is the bank angle, and m is the
mass of the vehicle.

The angular kinematics are defined by

$$
\begin{aligned}
\dot{\sigma} &= p \cos(\alpha) \sec(\beta) + r \sin(\alpha) \sec(\beta) \\
\dot{\alpha} &= -p \cos(\alpha) \tan(\beta) + q - r \sin(\alpha) \tan(\beta) \\
\dot{\beta} &= p \sin(\alpha) - r \cos(\alpha)
\end{aligned}
\tag{4}
$$

where p, q, and r are the angular velocities about the body-fixed x, y, and z axes respectively, α is the angle
of attack and β is the sideslip angle.

The linear kinematics are given by

$$
\begin{aligned}
\dot{z} &= V \sin(\gamma) \\
\dot{\Phi} &= \frac{V}{z} \cos(\gamma) \cos(\xi) \\
\dot{\lambda} &= \frac{V}{z \cos(\Phi)} \cos(\gamma) \sin(\xi)
\end{aligned}
\tag{5}
$$

where Φ and λ are the latitude and longitude of the vehicle, respectively.

For the vehicle integrated with aerodynamic control surfaces, the angular dynamics are given by

$$
\begin{bmatrix} \dot{p} \\ \dot{q} \\ \dot{r} \end{bmatrix} = \left(\mathbb{I}_b^{B/B_{cm}} \right)^{-1} \left(\begin{bmatrix} \mathcal{L} \\ \mathcal{M} \\ \mathcal{N} \end{bmatrix} - \begin{bmatrix} p \\ q \\ r \end{bmatrix} \times \mathbb{I}_b^{B/B_{cm}} \begin{bmatrix} p \\ q \\ r \end{bmatrix} \right)
\tag{6}
$$

American Institute of Aeronautics and Astronautics

where $\mathbb{I}_b^{B/B_{cm}}$ is the inertia tensor of the vehicle about its center of mass (COM) expressed in the body coordinates and $\mathcal{L}$, $\mathcal{M}$, and $\mathcal{N}$ are the aerodynamic roll, pitch, and yaw moments, respectively.

For the vehicle integrated with reaction control systems, the angular dynamics are given by

$$\begin{bmatrix} \dot{p} \\ \dot{q} \\ \dot{r} \end{bmatrix} = \left(\mathbb{I}_b^{B/B_{cm}} \right)^{-1} \left(\begin{bmatrix} \mathcal{L} \\ \mathcal{M} \\ \mathcal{N} \end{bmatrix} + \begin{bmatrix} \mathcal{L}_{RCS} \\ \mathcal{M}_{RCS} \\ \mathcal{N}_{RCS} \end{bmatrix} - \begin{bmatrix} p \\ q \\ r \end{bmatrix} \times \mathbb{I}_b^{B/B_{cm}} \begin{bmatrix} p \\ q \\ r \end{bmatrix} \right) \tag{7}$$

where $\mathcal{L}_{RCS}$, $\mathcal{M}_{RCS}$, and $\mathcal{N}_{RCS}$ are the roll, pitch, and yaw torques, respectively, generated by the reaction control thrusters.

For the moving mass system, the angular dynamics are derived from the angular momentum equation:

$$\begin{bmatrix} \mathcal{L} \\ \mathcal{M} \\ \mathcal{N} \end{bmatrix} = {}^{I}\frac{d}{dt} \, {}^{I}H^{S/S^*} \tag{8}$$

where ${}^{I}H^{S/S^*}$ is the angular momentum of the total vehicle system (including all movable masses), S, in the inertial reference frame, I, about the total vehicle center of mass S^*. This can be expressed in terms of the movable mass positions and inertial velocities,

$$ {}^{I}H^{S/S^*} = I^{B/B^*} \, {}^{I}\omega^B + \sum \delta_i \times m_i \, {}^{I}v^{\delta_i} - \frac{1}{m_S} \left(\sum m_i \delta_i \right) \times \left(m_B \, {}^{I}v^{B^*} + \sum m_i \, {}^{I}v^{\delta_i} \right) \tag{9}$$

where m_i is the ith movable mass, m_B is the mass of the PBV without movable masses, m_S is the mass of the PBV with all movable masses, I^{B/B^*} is the inertia dyad of the PBV body, B, without movable masses, about the center of mass of B, denoted B^*. δ_i is the position of the ith movable mass from B^* in the B fixed coordinate system, with $\dot{\delta}_i$ and $\ddot{\delta}_i$ used to indicate the first and second time-derivatives in the B-fixed coordinate system. ${}^{I}v^{B^*}$ is the velocity of point B^* in the inertial frame and ${}^{A}\omega^B$ is the angular velocity of the B reference frame with respect to the inertial frame.

The derivative of the angular momentum on the right hand side of Eq. 8 produces the desired angular accelerations $\dot{p}$, $\dot{q}$, and $\dot{r}$. This equality can then be solved for the desired derivatives, resulting in the angular dynamics equations for the vehicle with the moving mass system:

$$\begin{aligned} \begin{bmatrix} \dot{p} \\ \dot{q} \\ \dot{r} \end{bmatrix} = & \left[I^{B/B^*} - \sum \left(m_i \delta_i \times (\delta_i \times + \frac{1}{m_S} \left(\sum m_i \delta_i \times \left(\sum m_i \delta_i \times \right) \right]^{-1} \left(\begin{bmatrix} \mathcal{L} \\ \mathcal{M} \\ \mathcal{N} \end{bmatrix} - \sum m_i \left(\dot{\delta}_i \times {}^{I}v^{\delta_i} \right) \right. \\ & - \sum m_i \left[\delta_i \times \left({}^{B}\frac{d}{dt} {}^{I}v^{B^*} + \ddot{\delta}_i + {}^{I}\omega^B \times \dot{\delta}_i \right) \right] \\ & + \frac{1}{m_S} \left(\sum m_i \dot{\delta}_i \right) \times \left(m_B \, {}^{I}v^{B^*} + \sum m_i \, {}^{I}v^{\delta_i} \right) \\ & + \frac{1}{m_S} \left(\sum m_i \delta_i \right) \times \left(m_B \, {}^{B}\frac{d}{dt} {}^{I}v^{B^*} + \sum m_i \left({}^{B}\frac{d}{dt} {}^{I}v^{B^*} + \ddot{\delta}_i + {}^{I}\omega^B \times \dot{\delta}_i \right) \right) \\ & \left. - {}^{I}\omega^B \times {}^{I}H^{S/S^*} \right) \end{aligned} \tag{10}$$

IV. Control Design

In this section, the controller designed for each vehicle control architecture using the simulation framework described in Section III is described. For each control hardware architecture, we design a linear multi-input multi-output (MIMO) optimal state feedback integral controller using Linear Quadratic Regulator techniques. The MIMO feedback controller is chosen because there are multiple guidance output commands for the controller to achieve using multiple control effector inputs and these input-output interactions must

be handled in a structured, optimal manner. All controllers are designed to be capable of tracking feasible guidance commands of angle of attack, sideslip angle, and bank angle (multi-output) using the different multi-inputs (eight flap deflection values for the FCS, four reaction thruster commands, on or off, for the RCS, and eight movable mass locations for the MMCS). The LQR approach also handles the control allocation effort and enables the direct mapping to control input for the different configurations, making this control design an attractive solution for the FCS, RCS, and MMCS configurations. For brevity, the MIMO LQR design approach using the FCS is describedd and relevant changes to the control design for the RCS & MMCS are noted.

For the flap control system, to provide the ability for the controller to track bank angle, angle of attack, or sideslip commands, the vehicle state is modeled as

$$x = [p \ q \ r \ \sigma \ \alpha \ \beta \ e_\sigma \ e_\alpha \ e_\beta]^T$$

These states include the angular velocity components and vehicle orientation parameters, defined in Section B and three additional augmented integral error state variables e_σ, e_α, and e_β. This augmentation is done to reduce steady-state errors between the actual and commanded bank angle, angle of attack, and sideslip. The derivatives for the integral error state variables are given by

$$\dot{e}_\sigma = \sigma - \sigma_c$$
$$\dot{e}_\alpha = \alpha - \alpha_c$$
$$\dot{e}_\beta = \beta - \beta_c$$

where α_c, β_c, and σ_c are the guidance commands. The system control inputs

$$u = [\delta_1 \ \delta_2 \ \cdots \ \delta_8]^T$$

are the hinge deflection angles of the eight aerodynamic control surfaces into or out of the flow. For the states defined above, we linearize the equations of motion, at a nominal point in the flight envelope to obtain state-space linear equations of the form

$$\Delta \dot{x} = A \, \Delta x + B \, \Delta u$$

where Δx and Δu are deviations from the linearization point x^*, u^*. The matrices A and B defined by

$$A = \left. \frac{\partial f}{\partial x} \right|_{x^*,u^*} \qquad B = \left. \frac{\partial f}{\partial u} \right|_{x^*,u^*}$$

are the state and input matrices respectively. Here, $f(x, u)$ is the vector-valued function of the derivatives for each state variable concatenated together.

The control law is given as

$$u = u^* - K \, \Delta x$$

where K is the feedback gain matrix, u^* is a nominal control surface configuration, and Δx is the state deviation from the nominal trim configuration. The gain K is computed to minimize the quadratic cost function

$$J = \int_0^\infty \Delta x^T(\tau) \, Q \, \Delta x(\tau) + \Delta u^T(\tau) \, R \, \Delta u(\tau) \, d\tau$$

where Q and R are tunable weighting matrices for the states and control surfaces respectively. Using the Q matrix, we can tune the peformance and responses of the state variables and by tuning the R matrix, we can define which and how much of a control variable to use.

For the RCS configuration, the state variables are identical to the FCS configuration but the system control inputs are reaction torques about the three body axes

$$u = [\mathcal{L}_{RCS} \ \mathcal{M}_{RCS} \ \mathcal{N}_{RCS}]^T$$

These reaction torque inputs are obtained using the LQR control design and are then mapped to the jet thrusters using a jet selection logic developed by Johnson et al [4]. The generalized jet selection algorithm takes inputs along with the LQR required torques to output ON/OFF commands. Before flight simulation, the jet selection tool is run to derive all torque combinations and pre-load into tables.

American Institute of Aeronautics and Astronautics

For the moving mass control configuration, since the velocities and accelerations of the movable masses enter the equations of motion as seen in Eq. 10, we model the vehicle state to include these velocities and accelerations as

$$x = \begin{bmatrix} p\ q\ r\ \sigma\ \alpha\ \beta\ e_\sigma\ e_\alpha\ e_\beta\ \delta_1\ \delta_2\ \cdots\ \delta_8\ \dot\delta_1\ \dot\delta_2\ \cdots\ \dot\delta_8 \end{bmatrix}^T$$

with the control input defined as the accelerations of the movable masses:

$$u = \begin{bmatrix} \ddot\delta_1\ \ddot\delta_2\ \cdots\ \ddot\delta_8 \end{bmatrix}^T$$

V. Stability & Trimmability Analysis

In this section, we present an overview of the stability of the PBV and evaluate the trimmable ranges using the FCS configuration. In-depth stability analyses of the PBV can be found in prior publications of the authors [14,15]. Thus, for brevity, the relevant static stability derivatives are summarized in Table 2 at a maximum dynamic pressure flight condition obtained from an initial nominal guidance trajectory developed in Ref. [1]. This flight condition corresponds to a Mach number of 32, dynamic pressure of 2492 Pa, angle of attack of -15 degrees, and zero sideslip. Although, the dihedral effect, $C_{\mathcal{L}_\beta}$, the pitch stiffness, $C_{\mathcal{M}_\alpha}$, and the yaw stiffness, $C_{\mathcal{N}_\beta}$ are all stable as seen in Table 2, the non-zero dihedral effect $C_{\mathcal{L}_\beta}$ implies that a non-zero sideslip angle will induce a roll moment on the vehicle. Thus, any control architecture that commands a non-zero sideslip angle as required by guidance, must also be capable of generating a roll moment to counteract and trim out the associated induced roll due to sideslip. This implies that the alpha-beta (α-β) guidance approach, which generates angle of attack and sideslip commands, will require control effectors capable of generating pitch moments for α, yaw moments for β, and roll moments to trim the induced roll.

Table 2. Static stability derivatives

Stability derivative	Value	Stability
$C_{\mathcal{L}_\beta}$	-8.6 × 10^{-5}	stable
$C_{\mathcal{M}_\alpha}$	-4.4 × 10^{-3}	stable
$C_{\mathcal{N}_\beta}$	4 × 10^{-3}	stable

The design of the FCS is to generate primarily pitch and yaw moments for α-β guidance. Also, the PBV ribs, which are the attachment points of the control surfaces, are not aligned with the body y-z axes. Thus, deflecting a control surface primarily for pitch will also generate a small yaw moment and vice versa. As a result of the roll-yaw coupling and control surfaces generating pitch and yaw simultaneously, the controllable angle of attack and sideslip ranges for the PBV using the FCS are significantly limited [14,15]. In Fig. 6, the sideslip trimmability at different angles of attack and Mach numbers are depicted. These ranges were acquired using a Newton-Raphson solver at different angle of attack and sideslip combinations, using thousands of randomly seeded starting tab configurations. As a caveat, these trim conditions are not necessarily unique and solutions depend on the initial conditions of the control surface deflections.

These results extend to the MMCS configuration as well, which has an even smaller range of pitch and yaw moment generation. The MMCS configuration generates smaller pitch and yaw moments due to the weight limitations and available travel distance along the ribs for the masses [12]. This restricts the α-β guidance bounds to ranges that reduce the precision targeting capability. The FCS and MMCS configurations of the PBV have limited ability to trim out roll induced by holding a sideslip, thus a guidance approach, such as bank angle guidance, which doesn't require holding a non-zero sideslip, must be considered. A bank angle command can be generated by yawing the vehicle and taking advantage of the induced roll generated by the yaw. The reason that bank-to-turn works and skid-to-turn doesn't is that a bank command needs to generate rolling torque only when the roll is changing (i.e. when the vehicle reaches the desired steady-state roll, no more rolling torque is required), whereas a sideslip command requires a constant reaction rolling torque from the FCS and MMCS. Thus, the approach for these two architectures in the rest of the paper, is to utilize the inherent coupling to track bank angle commands by instantaneously commanding, but not holding, a sideslip angle. The RCS continues to be used directly as designed for bank angle guidance tracking through the reaction thrusters.
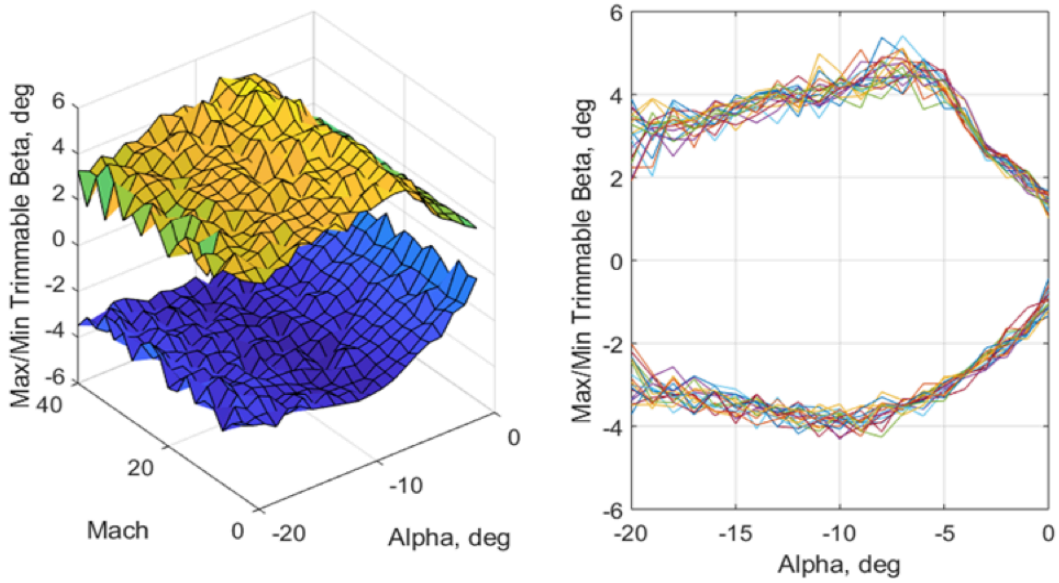
American Institute of Aeronautics and Astronautics

Figure 6. Trimmable Regions (a) Surface View (b) Trimmability Curves for Different Machs

VI.   Yaw-to-Bank Design and Evaluation

For the FCS and MMCS, the core controls group developed a novel yaw-to-bank control architecture to leverage the roll-yaw coupling and achieve high performance bank control. In this approach, the control design is decomposed into an inner and outer loop. The outer control loop tracks bank angle commands by commanding the appropriate sideslip which induces a roll moment through the dihedral effect. The inner control loop tracks (i) angle of attack commands from guidance including regulation about a constant angle of attack and (ii) sideslip commands generated by the outer control loop. A block diagram of this architecture is shown Figure 7.
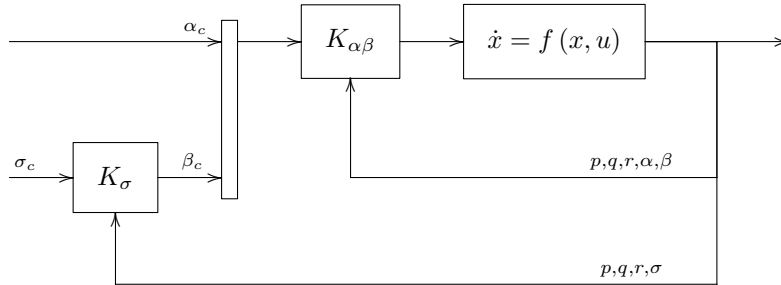

Figure 7. Yaw to bank control block diagram

To make a quick assessment of the bank angle tracking capability across the FCS, RCS, and MMCS architectures, we select the maximum bank acceleration attainable by the control system, as an indicator of maneuverability and a metric for control system performance. The dihedral derivative, $C_{\mathcal{L}_\beta}$, quantifies the amount of roll moment, $\mathcal{L}$, that is induced by a sideslip angle, β. This roll moment in turn affects the angular acceleration about the body x axis, $\dot{p}$, as seen in the angular dynamics equations in Section B. Taking the derivative of the bank angle rate, Eq. 4, introduces the body roll acceleration, $\dot{p}$, into the bank angle acceleration, $\ddot{\sigma}$, as seen in Eq. 11. Although both the bank rate and acceleration, in Eqs. 4 and 11 respectively, also dependent on the yaw rate, $\dot{r}$, rigid flight vehicle dynamics, demonstrate that bank is more related to roll than yaw as a roll is a rotation about the vehicle's body x axis while bank is a similar rotation about the velocity vector. Thus, for small angles of attack, the $\dot{p}$ term dominates and is the primary determinant of the bank acceleration.

American Institute of Aeronautics and Astronautics

$$\ddot{\sigma} = \dot{p}\cos(\alpha)\sec(\beta) - p\sin(\alpha)\,\dot{\alpha}\sec(\beta) + p\cos(\alpha)\sec(\beta)\tan(\beta)\,\dot{\beta}$$
$$+ \dot{r}\sin(\alpha)\sec(\beta) + r\cos(\alpha)\,\dot{\alpha}\sec(\beta) + r\sin(\alpha)\sec(\beta)\tan(\beta)\,\dot{\beta} \tag{11}$$

These dependencies demonstrate that the maximum sideslip angle that can be reached by the FCS or MMCS is an indicator of (i) roll control authority through the dihedral effect, (ii) bank acceleration, and thus (iii) bank maneuverability of the two architectures. Therefore, an estimate for the maximum bank acceleration of these two control systems, is the largest sideslip magnitude that can be achieved by the control system. This maximum sideslip can be obtained by solving for the sideslip at the maximum yaw configuration for the vehicle. For the FCS, the flaps on one side of the $x-z$ plane are deflected out of the flow to the maximum retraction limit and the others are deflected into the flow to the maximum. For the MMCS, the masses are moved all the way out on side and moved all the way in on the other side of the $x-z$ plane to generate the maximum yaw. Since the trim angle of attack, sideslip, and induced roll moment depend on the flight condition, this analysis was performed and the control capability metric evaluated at two different points in the flight envelope: (i) guidance and control initiation point and (ii) maximum dynamic pressure location. The roll moment and bank acceleration of the RCS is independent of flight condition and is simply determined by the position, orientation, and impulse capability of the thruster jets. The results are shown in Table 3.

Table 3. Control Capability Comparison Across Architectures

parameter	FCS		MMCS		RCS
	max $\bar{q}$	G&C act	max $\bar{q}$	G&C act	
M	32	39	32	39	–
$\bar{q}$ (Pa)	2896	284	3021	298	–
α (deg)	-10.65	-10.41	-11.10	-10.96	-16.28
β (deg)	-19.39	-19.38	-7.40	-7.32	–
$\ddot{\sigma}$ (deg/s^2)	115	11.5	13.8	1.48	10.9
$\mathcal{L}$ (Nm)	12.9	1.20	1.46	1.36×10^{-1}	0.84
$\mathcal{M}$ (Nm)	1.54×10^{-6}	1.7×10^{-7}	5.23×10^{-7}	4.46×10^{-8}	-4.02×10^{-3}
$\mathcal{N}$ (Nm)	-2.04×10^{-6}	-2.3×10^{-7}	-1.88×10^{-6}	-1.29×10^{-7}	-8.51×10^{-6}

Table 3 shows the Mach number, M, dynamic pressure, $\bar{q}$, angle of attack, α, sideslip, β, and bank acceleration, $\ddot{\sigma}$, along with the pitch, roll, and yaw moments for the FCS, RCS, and MMCS vehicle architectures when the vehicle is at the maximum yaw right orientation. For the FCS and MMCS, these parameters are presented at maximum dynamic pressure and G&C activation while for the RCS, the maximum bank angle acceleration remains constant throughout the trajectory. Table 3 demonstrates that the maximum sideslip angle using the FCS is significantly larger than that obtained from the MMCS. This impacts the bank acceleration results for which the FCS is capable of generating bank accelerations almost ten times the capability of the MMCS. For good bank angle guidance performance for the chosen reference design mission [1], a control system should be capable of achieving at least 5 deg/s/s bank acceleration rates [5]. At G&C activation, the MMCS falls short of this constraint, implying that certain bank maneuvers to achieve precision targeting may not be attainable using this control configuration. Both the FCS and RCS configurations are capable of meeting the constraints with the FCS having over ten times the RCS bank acceleration capability at maximum dynamic pressure.

To that effect, we simulate responses to two different bank angle guidance trajectories developed for the baseline vehicle integrated with the two different control architectures - FCS and RCS. Figs. 8 and 9 show the vehicle tracking response using the FCS and RCS respectively. In Fig. 8 the angle of attack, sideslip, and bank angle commands and responses along with the control surface deflections required to track the commands are plotted. The sideslip is observed to change to generate a roll moment in accordance with the outer loop bank angle command as described in the "yaw-to-bank" design framework. When no change in the bank angle is required, the sideslip is maintained at zero degrees, a tractable orientation for the control surfaces to achieve. Furthermore, the angle of attack is held at a fixed value as there is no angle-of-attack modulation required to correct downrange as in the $\alpha - \beta$ guidance scheme. Furthermore, the control

surfaces stay well within their saturation limits with control surfaces 7 and 8 at their maximum retraction angle of 45 degrees out of the flow. This indicates that for this vehicle, FCS configuration, and guidance trajectory requirements, fewer than 8 flaps are sufficient for control. Towards the end of the trajectory, slight oscillations in the sideslip angle are observed with reduced tracking performance in angle of attack. This may be rectified with better tuning or gain scheduling of the control gains as the gains were obtained for the PBV with FCS operating at an earlier point in the trajectory. Fig. 9 also shows good tracking of the bank angle commands using the RCS architecture, which is expected given its bank acceleration capability. Both designs are promising and provide the capability of tracking bank angle guidance commands for the vehicle and ensuring precision targeting.
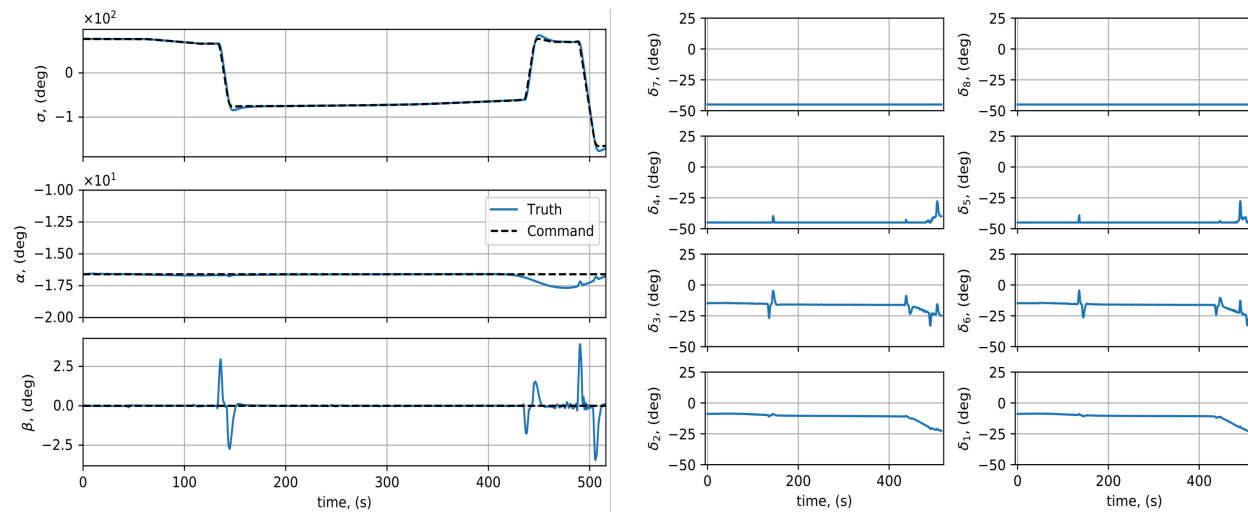

Figure 8. Bank angle tracking using FCS (i) angle of attack, sideslip, and bank angle (ii) control surface deflections, 1 - 8
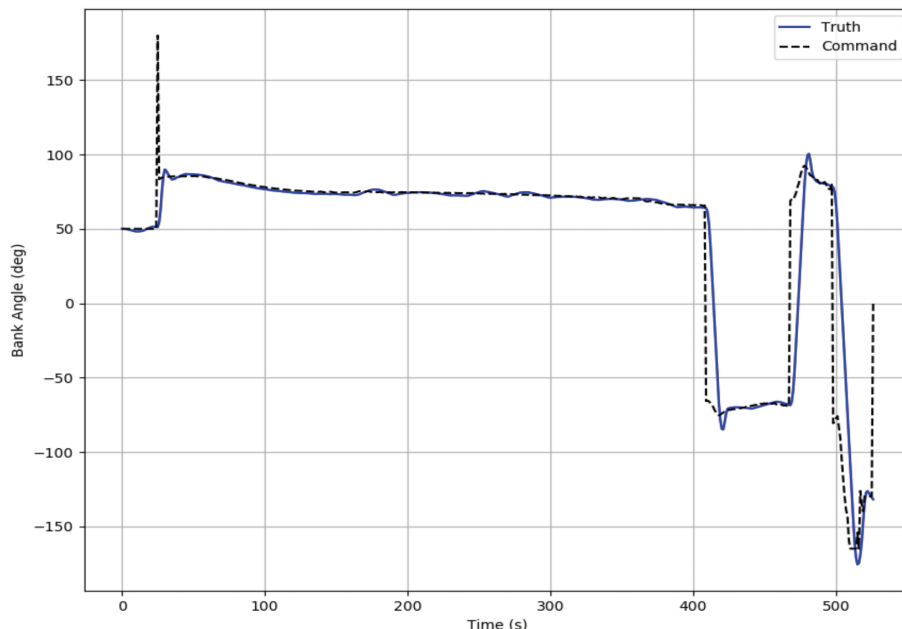

Figure 9. Bank angle tracking using RCS

American Institute of Aeronautics and Astronautics

VII.   Conclusion & Future Work

In this paper, we investigated three different control architectures for a Deployable Entry Vehicle (DEV) - aerodynamic control surfaces/flaps (FCS), reaction control systems (RCS), and moving mass control system (MMCS). These designs were independently integrated on the vehicle to generate moments that will enable tracking (i) heritage bank angle guidance commands for lift modulation & coupled downrange/crossrange control and (ii) unconventional angle of attack, α, and sideslip, β, guidance commands for independent downrange and crossrange control. The novel and unconventional FCS and MMCS architectures were designed to track $\alpha - \beta$ guidance commands while the RCS was designed to track heritage bank angle commands. It was discovered that the asymmetric DEV under investigation, had a non-zero induced roll due to sideslip that the FCS and MMCS architectures had limited capability to handle for the chosen mission. These two architectures were designed to provide independent angle of attack and sideslip commands with limited consideration for roll moment generation to trim. As a result, for this vehicle configuration, the FCS and MMCS configurations as designed, could not provide the control authority to track $\alpha - \beta$ guidance commands.

Similar to the RCS control objectives, the FCS and MMCS were then utilized to track bank angle guidance commands by taking advantage of the roll induced by briefly commanding but not holding a sideslip. A measure of bank angle tracking capability, the maximum bank acceleration, was developed and investigated to evaluate and compare the three architectures. The results showed that the FCS had the largest bank angle acceleration in comparison the other two - RCS and MMCS. It was also demonstrated that the FCS and RCS had the control authority to generate bank accelerations that exceeded the minimum required for good performance and trajectory tracking while the MMCS did not meet the requirement. For this vehicle, sample mission, mechanical design limitations, and control configurations as designed, the FCS architecture is the most promising in achieving good trajectory tracking results. Future work will involve a robustness analysis of the control design, investigation of the FCS performance at the later points in the flight envelope, and possible gain scheduling to improve performance and reduce dither. In addition, a different PBV will be studied to develop the $\alpha - \beta$ guidance and control G&C scheme for a DEV with reduced roll-yaw coupling and demonstrate the feasibility of the novel G&C architecture for a more conventional DEV configuration.

Acknowledgments

References

[1] D'Souza, S. N., Okolo, W. A., Nikaido, B. E., Yount, B. C., Tran, J., Margolis, B. W. L., Smith, B. P., Cassell, A. M., Johnson, B. J., Hibbard, K. E., Barton, J. D., and Hays, Z., "Developing an Entry Guidance and Control Design Capability using Flaps for the Lifting Nano-ADEPT," *AIAA Aviation and Aeronautics Forum and Exposition*, 2019.

[2] D'Souza, S. N. and Sarigul-Klijn, N., "Survey of Planetary Entry Guidance Algorithms," *Journal of Progress in Aerospace Sciences*, Vol. 68.

[3] Okolo, W., Dogan, A., and Blake, W., "Alternate trimming methods for trailing aircraft in formation flight," *Journal of Guidance, Control, and Dynamics*, Vol. 38, No. 10, 2015, pp. 2018–2025.

[4] Johnson, B. J., Cerimele, C. J., Stachowiak, S., Sostaric, R. R., Matz, D. A., and Lu, P., "Mid-lift-to-drag ratio rigid vehicle control system design and simulation for human Mars entry," *2018 AIAA Guidance, Navigation, and Control Conference*, 2018, p. 0615.

[5] JJohnson, B. J., Rocca-Bejar, D., Lu, P., Nikaido, B. E., Yount, Bryan C., D. S. N., and Hays, Z. B., "Pterodactyl: Development and Performance of Guidance Algorithms for a Mechanically Deployed Entry Vehicle," *AIAA SciTech 2020 Forum*, AIAA, Orlando, FL, January 2020.

[6] Widnall, W. S., "The minimum-time thrust-vector control law in the Apollo lunar-module autopilot," *IFAC Proceedings Volumes*, Vol. 3, No. 1, 1970, pp. 136–153.

[7] Martin, F. H. and Battin, R. H., "Computer-controlled steering of the Apollo spacecraft." *Journal of Spacecraft and Rockets*, Vol. 5, No. 4, 1968, pp. 400–407.

[8] Alunni, Antonella I., D. S. N. Y. B. C. O. W. A. M. B. W. N. B. E. J. B. J. B. J. D. L. G. W. L. and Hays, Z., "Pterodactyl:

Trade Study for an Integrated Control System Design of a Mechanically Deployable Entry Vehicle," *AIAA SciTech 2020 Forum*, AIAA, Orlando, FL, January 2020.

[9]Directorate, N. S. T. M., "Center Innovation Fund 2016 Winners Nano-ADEPT Lifting: Design Development for a Lifting Flight Test Demonstration," 2016.

[10]Directorate, N. S. T. M., "Adaptable, Deployable, Entry, and Placement Technology (ADEPTSR-1)," 2019.

[11]Cassell, A., Smith, B., Wercinski, P., Ghassemieh, S., Hibbard, K., Nelessen, A., and Cutts, J., "ADEPT, A Mechanically Deployable Re-Entry Vehicle System, Enabling Interplanetary CubeSat and Small Satellite Missions," *32nd Annual AIAA/USU Conference on Small Satellites*, SSC18-XII-08, Utah, August 2018.

[12]Yount, B. C., Cassell, A. M., and D?Souza, S. N., "Pterodactyl: Mechanical Designs for Integrated Control Design of a Mechanically Deployed Entry Vehicle," *AIAA SciTech 2020 Forum*, AIAA, Orlando, FL, January 2020.

[13]Nikaido, B. E., D'Souza, S. N., Hays, Z. B., and Reddish, B. J., "Pterodactyl: Aerodynamic and Aeroheating Database Development for Integrated Control Design of a Mechanically Deployed Entry Vehicle," *AIAA SciTech 2020 Forum*, AIAA, Orlando, FL, January 2020.

[14]Margolis, B. W., Okolo, W. A., Nikaido, B. E., Barton, J. D., and D'Souza, S. N., "Control and Simulation of a Deployable Entry Vehicle with Aerodynamic Control Surfaces," *Astrodynamics Specialist Conference*, 2019.

[15]Margolis, B. W., Okolo, W. A., and D'Souza, S. N., "Control Design & Sensitivity Analysis for a Deployable Entry Vehicle with Aerodynamic Control Surfaces," *International Astronautical Congress*, 2019.

[16]de Boor, C., *A Practical Guide to Splines*, Springer, 1978.

[17]W. L. Margolis, B. and Lyons, K., "ndsplines: A Python Library for Tensor-Product B-Splines of Arbitrary Dimension," *Journal of Open Source Software*, Vol. 4, No. 42, 10 2019, pp. 1745.

[18]Vinh, N. X., Busemann, A., and Culp, R. D., *Hypersonic and Planetary Entry Flight Mechanics*, The University of Michigan Press, Ann Harbor, 1980.

American Institute of Aeronautics and Astronautics